

Diffuse interface model to simulate the rise of a fluid droplet across a cloud of particles

Gregory Lecrivain,^{1,2,*} Yuki Kotani,^{1,2} Ryoichi Yamamoto,² Uwe Hampel,^{1,3}
and Takashi Taniguchi^{2,†}

¹*Helmholtz-Zentrum Dresden-Rossendorf, Institut für Fluidodynamik, Bautzner Landstraße 400,
01328 Dresden, Germany*

²*Kyoto University, Department of Chemical Engineering, Kyoto 615-8510, Japan*

³*Technische Universität Dresden, AREVA-Stiftungsprofessur für Bildgebende Messverfahren für die Energie-
und Verfahrenstechnik, 01062 Dresden, Germany*



(Received 1 March 2018; published 25 September 2018)

A large variety of industrial and natural systems involve the adsorption of solid particles to the fluidic interface of droplets in motion. A diffuse interface model is here suggested to directly simulate the three-dimensional dynamics of a fluid droplet rising across a cloud of large particles. In this three-phase model the two solid-fluid boundaries and the fluidic boundary are replaced with smoothly spreading interfaces. The capillary effects and the three-phase flow hydrodynamics are fully resolved. A special treatment is adopted for the interparticle collisions. The effect of the particle concentration on the terminal velocity of a rising fluid droplet is then investigated. It is found that, at low Reynolds number, the terminal velocity of a rising fluid droplet decreases exponentially with the particle concentration. This exponential decay is confirmed by a simple rheological model.

DOI: [10.1103/PhysRevFluids.3.094002](https://doi.org/10.1103/PhysRevFluids.3.094002)

I. INTRODUCTION

A large variety of systems involve the adsorption of solid particles to the fluidic interface of droplets in motion. Important industrial applications include the stabilization of emulsions and foams [1], the armoring of droplets moving in capillary tubes [2], along with the recovery of mineral particles by rising gas bubbles [3,4]. The encapsulation of oceanic air bubbles in a stabilizing organic film of particles is also remarkable phenomenon, for which the addition of a solid constituent drastically changes the dynamics of a natural binary fluid system [5]. The direct numerical simulation of such ternary systems is difficult. This can probably be attributed to the complexity of the mechanism itself, in which capillary effects, three-phase flow hydrodynamics, and interparticle collisions are all intertwined. The majority of the developed three-phase models were used to primarily test the dynamics of a single particle trapped at a planar fluidic interface [6–8]. Some more complex simulations were also performed to study the rearrangement of ellipsoidal particles initially placed at the fluidic interface of an immobile spherical droplet [9,10]. When it comes to simulating the rise of a droplet across a cloud of particles, only a few attempts can be found in the literature. We cite, for instance, the work of van Sint Annaland *et al.* [11], in which the dynamics of a rising gas bubble interacting with a large cloud of pointlike particles were simulated. Sasic *et al.* [12] later suggested particle-resolved simulations in a relatively small ternary system, typically containing no more than five particles. More recently, Bogner *et al.* [13] reported

*g.lecrivain@hzdr.de

†taniguch@cheme.kyoto-u.ac.jp

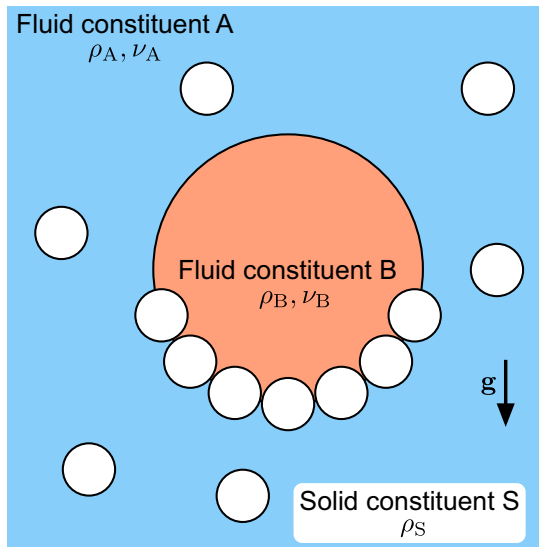


FIG. 1. Schematic of the reference ternary system representing a fluid droplet B rising in the host fluid A. The particles of the solid constituent S adsorb at the fluidic interface of the binary fluid.

particle-resolved simulations of a much larger system, thereby pointing out the growing importance of fully resolved three-phase flow simulations. In a similar way, the aim of this work is the fully resolved and three-dimensional simulation of a rising fluid droplet in a multiparticle system. The diameter of each particle spreads over 10 grid points and that of the bubble over about 50 points. The simulations are performed using a modified diffuse interface model, meaning that the fluidic boundary and the two solid-fluid boundaries are replaced with smoothly spreading interfaces [14]. The three-phase diffuse interface model extends on formulations previously proposed [15–18]. After suggesting an appropriate treatment for the interparticle collisions, found to adversely affected by the diffusivity of the solid-fluid interface, the effect of particle concentration on the terminal velocity of a rising droplet is investigated.

II. SIMULATION MODEL

A. Binary fluid mixture

Suppose a ternary system, in which a dispersed solid constituent representing the particle cloud is immersed in a binary fluid mixture. A schematic of the reference ternary system presently investigated is illustrated in Fig. 1. The capital letter “S” is hereafter introduced to denote a quantity associated with the solid constituent. The field $\phi_S(\mathbf{x}, t)$, where \mathbf{x} is the spatial coordinate and t the time, denotes the volume fraction of the solid constituent. The binary fluid mixture separates into its two immiscible fluid constituents, “A” and “B.” The constituent A represents the host fluid and the constituent B the fluid inside the droplet. In a similar fashion, the two volume fractions $\phi_A(\mathbf{x}, t)$ and $\phi_B(\mathbf{x}, t)$ are also introduced. The separation of the binary fluid mixture into its two constituents is driven by the minimization of the free energy

$$\mathcal{F} = \frac{k_B T_0}{v_0} \int_{\mathcal{V}} f(\phi_A, \phi_B, \phi_S) d\mathbf{x}, \quad (1)$$

where \mathcal{V} is the region of space occupied by the ternary system, k_B the Boltzmann constant, T_0 the temperature, v_0 a reference unit volume, and f the free energy density scaled by the reference value $e_0 = k_B T_0 / v_0$. The formulation recently suggested by the same authors is here retained for the free

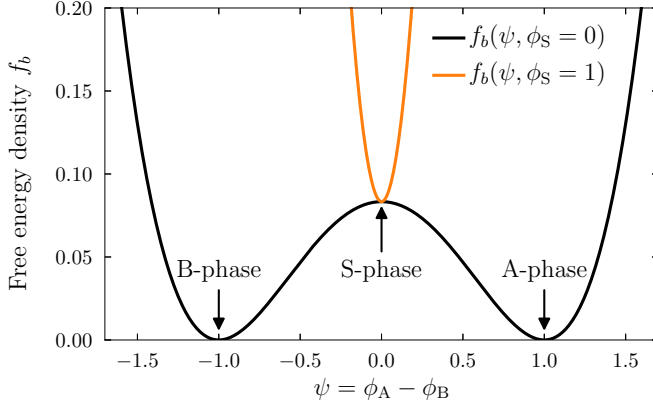


FIG. 2. Bulk component of the free energy density $f_b(\psi, \phi_S)$ inside and outside the solid constituent.

energy density [19,20]. The reader is referred to Appendix A for its exact formulation. Because of the phase summation $\phi_A + \phi_B + \phi_S = 1$, the free energy density is rewritten as $f(\psi, \phi_S)$, where this order parameter is defined as $\psi(\mathbf{x}, t) = \phi_A - \phi_B$. The value of this parameter ψ is obtained from the minimization of the free energy. The bulk component of the free energy density $f_b(\psi, \phi_S)$ is shown in Fig. 2.

Outside of the particle (i.e., $\phi_S = 0$), the free energy has two stable minima. The first minimum is located at $\psi = -1$ (fluid constituent B) and the second minimum at $\psi = 1$ (fluid constituent A). Inside the particle (i.e., $\phi_S = 1$), the free energy changes to a single well function with a minimum located at $\psi = 0$ (solid constituent S). This field ψ is updated in time according to the modified Cahn-Hilliard equation [17]

$$\frac{\partial \psi}{\partial t} + \nabla \cdot [\psi \mathbf{u} - M(\mathbf{I} - \mathbf{n}_S \otimes \mathbf{n}_S) \cdot \nabla \mu] = 0, \quad (2)$$

where M is the mobility, \mathbf{I} the unit tensor, $\mathbf{n}_S = -\nabla \phi_S / |\nabla \phi_S|$ the local unit vector normal to the surface of the solid particle, and $\mu(\psi, \phi_S) = \delta \mathcal{F} / \delta \psi$ the chemical potential. Away from the particle diffuse interface the outer product $\mathbf{n}_S \otimes \mathbf{n}_S$ is set to the zero tensor.

B. Solid constituent

The solid particle cloud forming the solid constituent S is decomposed into a number N_S of spherical particles with identical radius r_s . The lowercase letter $s \in S$ is hereafter used to denote a quantity associated with the s th Lagrangian particle. As one moves from the inner particle region to the outer region, the volume fraction ϕ_s of the s th particle smoothly transitions from unity to zero. A number of smooth profiles are suggested in Ref. [21]. A truncated hyperbolic function, associated with the interfacial distance ξ_S and the cutoff length ξ_c , is presently used to represent the spherical shape of each particle. The exact mathematical expression for $\phi_s(\mathbf{x}, t)$ can be seen in Eq. (B1) of Appendix B. Note that the cutoff length is primarily introduced to speed up the calculation time because it reduces the number of times the hyperbolic function is called. The total volume fraction of the solid constituent is then given by

$$\phi_S(\mathbf{x}, t) = \sum_{s \in S} \phi_s. \quad (3)$$

C. Hydrodynamics

The total velocity field is resolved using the “smooth profile method,” which essentially uses a Cartesian grid to solve the Navier-Stokes equations. In this method the total velocity field is decomposed as $\mathbf{u} = (1 - \phi_S)\mathbf{u}_{AB} + \phi_S\mathbf{u}_S$, where the first term is the velocity field of the binary fluid and the second term the solid velocity field. This latter is defined as $\phi_S\mathbf{u}_S = \sum \phi_s[\mathbf{V}_s + \boldsymbol{\Omega}_s \times (\mathbf{x} - \mathbf{X}_s)]$. Further reading on the smooth profile method can be found in Refs. [21,22]. The total velocity, which satisfies the incompressibility condition $\nabla \cdot \mathbf{u} = 0$, is here given by solving the modified momentum equation

$$\rho \left[\frac{\partial \mathbf{u}}{\partial t} + (\mathbf{u} \cdot \nabla) \mathbf{u} \right] = \nabla \cdot [-p\mathbf{I} + \boldsymbol{\sigma}_v] + \rho \phi_S \mathbf{f}_S + \mathbf{f}_c + \mathbf{f}_g, \quad (4)$$

where $\boldsymbol{\sigma}_v$ is the viscous stress tensor. The first additional term \mathbf{f}_S on the right-hand side of Eq. (4) enforces the particle rigidity. Its exact formulation can be found in the original development of the smooth profile method [21,22]. The second capillary term is given by $\mathbf{f}_c = -\psi \nabla \mu - \phi_S \nabla \mu_S$, where $\mu_S = \delta \mathcal{F} / \delta \phi_S$ [19]. The third gravity term is given by $\mathbf{f}_g = (\rho - \rho_{\text{avg}})\mathbf{g}$. The subtraction by the space-averaged density $\rho_{\text{avg}} = \int \rho(\mathbf{x}, 0) d\mathbf{x} / \int d\mathbf{x}$ was previously suggested for buoyancy-driven droplet flows in a periodic domain [23]. The total density and viscosity fields are given by

$$\rho(\mathbf{x}, t) = \phi_A(\mathbf{x}, t)\rho_A + \phi_B(\mathbf{x}, t)\rho_B + \phi_S(\mathbf{x}, t)\rho_S, \quad (5)$$

$$\eta(\mathbf{x}, t) = \phi_A(\mathbf{x}, t)\eta_A + \phi_B(\mathbf{x}, t)\eta_B + \phi_S(\mathbf{x}, t)\eta_S, \quad (6)$$

where the constants $\rho_{i=A,B,S}$ and $\eta_{i=A,B,S}$ are the respective user-defined density and viscosity of each constituent. Note that the two volume fractions ϕ_A and ϕ_B do not actually appear in our implementation, since we introduced the order parameter $\psi(\mathbf{x}, t)$. Hence the viscosity and the density fields are rewritten as $\rho(\psi, \phi_S)$ and as $\nu(\psi, \phi_S)$, respectively. The exact formulations are shown in Appendix C.

D. Multiparticle dynamics

The hydrodynamic force \mathbf{F}_{hyd} , the capillary force \mathbf{F}_{cap} , the collision force \mathbf{F}_{col} , and an external force \mathbf{F}_{ext} acting on each particle are presently retained. The equations for the translational velocity $\mathbf{V}_s = d\mathbf{X}_s/dt$, where \mathbf{X}_s is the position of the s th particle center of mass, and the rotational velocity $\boldsymbol{\Omega}_s$ are given by [24]

$$m_s \frac{d\mathbf{V}_s}{dt} = \mathbf{F}_{\text{hyd}} + \mathbf{F}_{\text{cap}} + \mathbf{F}_{\text{col}} + \mathbf{F}_{\text{ext}}, \quad (7)$$

$$\mathbf{I}_s \frac{d\boldsymbol{\Omega}_s}{dt} = \mathbf{T}_{\text{hyd}} + \mathbf{T}_{\text{cap}}, \quad (8)$$

where $m_s = \rho_S \int \phi_s d\mathbf{x}$ is the particle mass and $\mathbf{I}_s = \rho_S \mathbf{I} \int \phi_s \ell_s^2 d\mathbf{x}$ the diagonal inertia tensor, and $\ell_s = \mathbf{x} - \mathbf{X}_s$ the distance vector from the particle center of mass to the spatial coordinate. The term \mathbf{T}_{hyd} is the hydrodynamic torque, and \mathbf{T}_{cap} the capillary torque. The hydrodynamic and the capillary components are directly resolved. Their values are calculated by using a momentum conservation between the solid constituent and the binary fluid mixture. A detailed description of the force and torque calculations can be seen in Appendix D.

1. Depletion layer adjacent to the particle boundary (S1)

The reference system presently studied is composed of a binary fluid mixture, whose fluid constituents A and B are ideally separated by a sharp interface, and by multiple hard-sphere particles S with radii r_s . In this work, however, the three interfaces A/B, A/S, and B/S are no longer sharp but are replaced with smoothly spreading interfaces of user-defined thicknesses, which correspond to

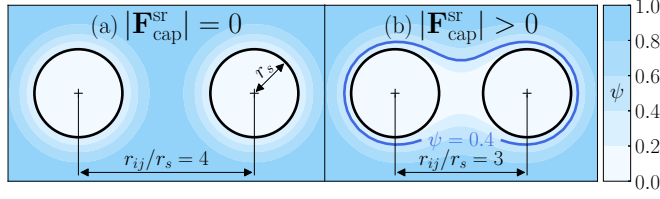


FIG. 3. Depletion layers adjacent to the boundaries of two solid particles immersed in the host consistent A (a). The two particles are pinned. Upon a close encounter, the depletion layers deform, and the two particles attract each other because of a short-range capillary force $\mathbf{F}_{\text{cap}}^{\text{sr}}$ (b).

given interfacial energies. Most of the particles are suspended in the host fluid. As one moves from the host fluid constituent A to the particle inner region S, the order parameter ψ smoothly transitions from unity to zero. This leads to the formation of a depletion layer across the solid particle boundary [Fig. 3(a)].

In a multiple particle system, as is the case here, this depletion layer induces an undesired capillary attraction. As two particles come close to each other, their respective depletion layers tend to locally deform [Fig. 3(b)]. Subsequently, a short-range capillary force $\mathbf{F}_{\text{cap}}^{\text{sr}}$ arises. This scenario, reminiscent of the liquid bridge bonding particles together [25,26], is an inevitable disadvantage occurring when working with a diffuse interface model. The distance, at which the short-range capillary force activates, here has a value comparable to that of the particle size, and so an affordable computational cost is achieved. The undesired effect caused by the short-range attraction force $\mathbf{F}_{\text{cap}}^{\text{sr}}$ can be further reduced by setting a smaller ratio of the interfacial thickness to the particle radius. Counteracting this short-range capillary attraction is a central aspect of this work. We suggest implementing the repulsive collision force acting on the i th particles as $\mathbf{F}_{\text{col}} = -(\mathbf{F}_{\text{cap}}^{\text{sr}} + \nabla U_{ij})$, where $\mathbf{F}_{\text{cap}}^{\text{sr}}$ is calculated using a preliminary set of simulations (detailed in the result section) and U_{ij} is a truncated Lennard-Jones potential [27]. The potential takes the form

$$U_{ij} = \begin{cases} 4\epsilon \left[\left(\frac{\sigma}{r_{ij}} \right)^{12} - \left(\frac{\sigma}{r_{ij}} \right)^6 \right] & \text{if } r_{ij} < r_c \\ 0 & \text{elsewhere} \end{cases}, \quad (9)$$

where ϵ is the depth of the potential well, $r_{ij} = |\mathbf{X}_i - \mathbf{X}_j|$ the separation distance between the center of masses of the i th and the j th particles, $\sigma = 2r_s + \xi_c$ the distance at which the interparticle potential equates zero, and $r_c = 2^{1/6}\sigma$ the cutoff distance. The truncation suppresses the attractive part of the potential.

III. RESULTS

The governing equations were implemented in their nondimensional form using the Reynolds number Re , the Péclet number Pe , and the capillary number Ca . These three nondimensional numbers are defined as

$$\text{Re} = \frac{\rho_0 U_0 L_0}{\eta_0}, \quad \text{Pe} = \frac{U_0 L_0}{D_0}, \quad \text{Ca} = \frac{\eta_0 U_0}{\gamma_0}, \quad (10)$$

where $\rho_0 = \rho_A$ and $\eta_0 = \eta_A$ are the density and the viscosity of the host fluid constituent A, respectively. The reference velocity is set to $U_0 = \sqrt{gL_0}$. The reference length is defined as $L_0 = \xi$, the diffusion coefficient as $D_0 = e_0 M$, and the reference surface tension as $\gamma_0 = e_0 L_0$. This nondimensionalization is similar to that used in previous studies on phase separation [28,29]. For the sake of conciseness, the procedure implemented to solve the governing equations is found in Appendix D. Using the present implementation, a fluid density ratio up to $\rho_A/\rho_B = 40$ can be achieved. The resulting droplet Reynolds and Eötvös numbers are calculated, based on the droplet radius r_b , as $\text{Re}_b = \rho_A r_b \sqrt{gr_b}/\eta_A = 0.98$ and $\text{Eo}_b = \rho_A g r_b^2/\gamma_0 = 0.23$ for all subsequent

TABLE I. Input parameters used in the simulation sets. The term Δ is the size of a grid element and N the number of grid nodes. In S3, S4, and S5, the Eötvös droplet numbers, Eo_b , and the Reynolds droplet number, Re_b , are set to constant values.

Binary fluid mixture							Solid constituent					Collision		Dimensionless numbers				Grid	
$\frac{\xi_A}{\xi}$	$\frac{\xi_B}{\xi}$	χ	$\frac{\rho_A}{\rho_B}$	$\frac{\eta_A}{\eta_B}$	$\frac{\tau_b}{\xi}$	$\frac{\xi_s}{\xi}$	$\frac{\xi_c}{\xi}$	$\frac{\rho_s}{\rho_A}$	$\frac{\eta_s}{\eta_A}$	$\frac{\nu_s}{\xi}$	N_S	$\frac{\sigma}{\xi}$	$\frac{\epsilon}{\gamma_0 \xi^2}$	Pe	Re_{100}	$\frac{Ca}{100}$	$\frac{\Delta}{\xi}$	N	
S1	1	1	8/3	[1-40]	1	18.3	-	-	-	-	0	-	-	1	1	5	1	128 ³	
S2	1	1	8/3	-	-	-	3	3.6	1	1	5	2	13.6	0.5	1	5	1	128 ³	
S3	1	1	8/3	10	1	[16,42.6]	3	3.6	1	1	[3.75,10]	22	[11.1,23.6]	0.5	1	[1.54,0.35]	[5.77,3.53]	1	[90 ² ,256 ²]
S4	1	1	8/3	10	1	26.6	3	3.6	1	1	6.25	[0-300]	16.1	0.5	1	0.72	4.47	1	160 ² , 160 ³
S5	1	1	8/3	10	1	[16-42.6]	3	3.6	1	1	[3.75-10]	22	[11.1,23.6]	0.5	1	[1.54-0.35]	[5.77-3.53]	1	[90 ² -256 ²]

simulations. These two numbers, commonly used to characterize the shape of rising gas bubbles in water [30], indicate that the rising droplet remains spherical throughout its ascension, thereby avoiding the ellipsoidal bubble regime. All the subsequent results are presented for two-dimensional and three-dimensional test cases.

A. Rising droplet in the absence of particles (S1)

First the terminal velocity of a rising droplet in a periodic domain is validated (simulation set S1). There are no particles in the system. The input parameters used in simulation set S1 are shown in Table I. In the Stokes regime, i.e., at low droplet Reynolds and Eötvös numbers, the spherical droplet only slightly deforms during its rise. This allows us to compare the simulated droplet terminal velocity $U_b^{\text{sim}} = \int \phi_B \mathbf{u} d\mathbf{x} / \int \phi_B d\mathbf{x}$ with its theoretical counterpart U_b^{th} [31,32]. The derivation of the theoretical terminal droplet velocity is described in Appendix E. Previous experimental and numerical data have shown that, up to a Reynolds number $Re_b < 2$, the drag coefficient of a spherical rising droplet is within the well-known drag curves for solid spheres and inviscid spherical bubbles, respectively $C_d = 24/Re_b$ and $C_d = 16/Re_b$ [33]. In the present investigated regime, the rising droplet remains fairly spherical. The Eötvös droplet number, $Eo_b < 1$, and the Reynolds droplet number, $Re_b < 2$, are set to low values. It is therefore fair to compare the data with a laminar Stokes drag, which we corrected due to the periodicity imposed on each side of the domain. Figure 4 shows the error in the droplet terminal velocity as a function of the fluid density ratio.

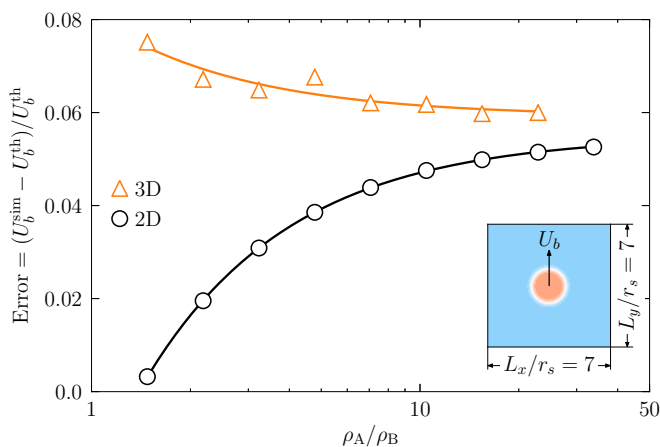


FIG. 4. Error in the terminal velocity of a rising spherical bubble in the absence of particles. Periodicity is enforced on all side boundaries of the domain.

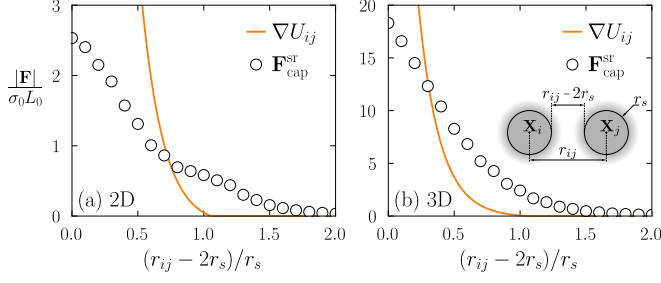


FIG. 5. Short-range capillary force $\mathbf{F}_{\text{cap}}^{\text{sr}}$ calculated as a function of the normalized particle separation distance r_{ij} . The two particles are pinned and immersed in the fluid constituent A. The repulsive force $-\nabla U_{ij}$ is also shown.

It is seen that a good agreement is achieved for $\rho_A/\rho_B > 10$. An error of about 6% is achieved in a two-dimensional and a three-dimensional domain. Note that the error is also dependent on the interfacial thicknesses ξ , ξ_A , and ξ_B [21]. Although it not shown here, the deformation of the droplet was also found to compare qualitatively well with the data of Hysing *et al.* [34] at higher capillary numbers.

B. Rising droplet in the presence of particles

1. Calculation of the short-range capillary force (S2)

At this stage the short-range capillary force $\mathbf{F}_{\text{cap}}^{\text{sr}}$ is still unknown. Hence a second of set of simulations S2, in which two pinned particles are immersed in the host fluid constituent A, is performed. As seen in Table I, the depth of the potential wall ϵ is arbitrarily set to a constant value throughout the subsequent simulations. Figure 5 shows the evolution of the short-range capillary force calculated as a function of the particle separation distance $r_{ij} - 2r_s$.

It is seen that the short-range capillary force decays exponentially with the separation distance. This finding is in line with previously reported data [17]. The magnitude of the repulsive force $-\nabla U_{ij}$, derived from the Lennard-Jones potential in Eq. (9), is also shown.

2. Suppression of the clustering effect (S3)

The effect of the corrected collision force $\mathbf{F}_{\text{col}} = -(\mathbf{F}_{\text{cap}}^{\text{sr}} + \nabla U_{ij})$ on a multiparticle system is here briefly tested in simulation set S3. At the initial time $t = 0$, the particles are randomly placed in the host fluid constituent A, and the droplet is placed at the center of the domain. The particles have the same density as that of the host fluid, i.e., $\rho_S/\rho_A = 1$. Figure 6 shows the effect of the corrected collision force on a multiparticle system.

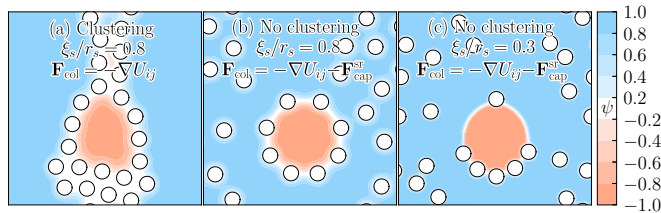


FIG. 6. Effect of the corrected collision force in a multiparticle system. In panel (a) clustering occurs as opposed to panel (b). The solid lines correspond to the reference particle radius r_s . In panel (c) the ratio of the interfacial thickness to the particle radius is decreased. The simulations are performed with $N_S = 23$ particles.

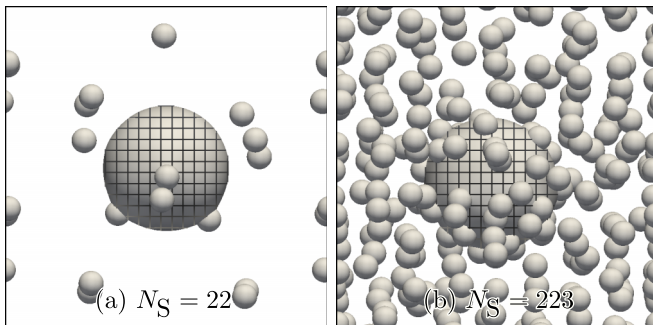


FIG. 7. Snapshot of the three-dimensional rising bubble in a multiparticle system: (a) low particle concentration; (b) high particle concentration.

In case (a), the collision force is too weak to overcome the short range capillary force, hence particle clustering occurs. In case (b), the clustering is suppressed. As expected the particles are eventually collected at the fluidic interface of the rising droplet. After the rising droplet is completely armored, the surrounding particles suspended in the host fluid constituent A were found to move around and avoid the rising particle-droplet aggregate. In case (c), the ratio of the interfacial thickness to the particle radius is decreased. A convergence study (Appendix F) showed that for a ratio below $\xi_s/r_s < 0.4$ the results become grid independent.

3. Effect of particle concentration (S4)

In simulation set S4, the number of particles suspended in the domain is varied. Figure 7 shows the three-dimensional rising droplet at low total solid fraction [Fig. 7(a)] and at high solid fraction [Fig. 7(b)]. See the Supplemental Material [35] for a typical animation of a droplet rising across a particle cloud.

The fluidic interface of the droplet is defined as the isosurface $\psi = 0$. The mean bubble velocity and its deviation are then calculated as a function of the number of particles. The statistics are averaged over two flow-through times, with one flow-through time being the time it takes for the droplet to traverse the domain height. Figure 8 shows the terminal velocity of the rising droplet as a function of the solid concentration in the host fluid.

The concentration of the solid constituent suspended in the host fluid, which essentially is a conversion of the number of particles suspended in A, is calculated as $\langle \phi_S \rangle = \int \phi_S d\mathbf{x} / \int \phi_A d\mathbf{x}$. It is found that the terminal velocity U_b of the droplet decreases exponentially with increasing solid concentration. This decrease is backed up quantitatively by the recent numerical and experimental

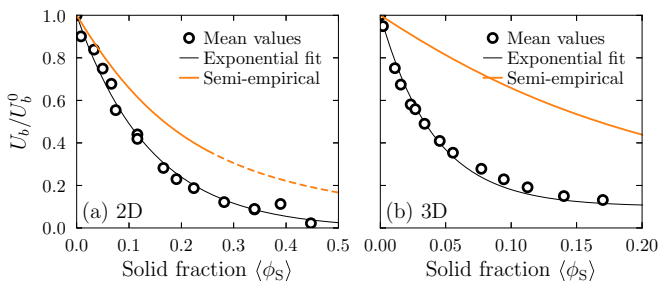


FIG. 8. Effect of the solid concentration in the host fluid on the terminal velocity of a rising bubble in the Stokes regime. The standard deviation of the mean bubble velocity is about as large as the symbols. The semiempirical expression, obtained with $\lambda_0 = 4$ and $\lambda_1 = 12$, is extrapolated beyond its range of validity.

observations [36,37]. For illustration purposes, an exponential fit was added to the figure. The exponential fit takes the form $U_b/U_b^0 = 1 - \alpha(1 - e^{-(\phi_S)/\beta})$, where α and β are two best-fit values, and U_b^0 equates the terminal velocity of the droplet in the absence of particles. With the present best-fit function, the droplet velocity ratio equals unity for $\langle\phi_S\rangle = 0$. With higher solid fraction, i.e., for $\langle\phi_S\rangle \rightarrow 1$, the droplet terminal velocity converges to the constant value $U_b/U_b^0 = 1 - \alpha$. In the present simulations, α equates to a value close to unity. It may, however, take a greater value, should the bubble move downwards because of the gravity. A direct comparison with data taken from the literature is difficult because the few available studies considered the rising of highly deformable air bubbles in water [37]. The simulations are here performed with a smaller density ratio. Based on a rheological model of Hooshyar *et al.* [36], we derive semiempirical values for the terminal droplet velocity rising across a suspension of particles. In the semidilute regime, i.e., for $\langle\phi_S\rangle < 0.25$, the apparent viscosity of the suspension A/S takes the polynomial form

$$\frac{\eta_{AS}}{\eta_A} = 1 + \lambda_0 \langle\phi_S\rangle + \lambda_1 \langle\phi_S\rangle^2, \quad (11)$$

where $1.5 < \lambda_0 < 5$ and $7.35 < \lambda_1 < 14.1$ [38]. In the dilute regime, restricted to $\langle\phi_S\rangle < 0.02$, the above equation simplifies to the well-established analytical expression $\eta_{AS}/\eta_A = 1 + 2.5\langle\phi_S\rangle$ [39]. By substituting the viscosity of the host fluid in Eq. (E1) with the apparent viscosity η_{AS} , a semiempirical terminal velocity can be estimated. While this semiempirical value does not take into account the particle attachment to the fluidic interface of the rising droplet, it does confirm the exponential decay presently observed.

IV. CONCLUSIONS

A diffuse interface model is suggested to directly simulate the dynamics of a rising droplet in the presence of large particles. An advantage of the method lies in the fact that the capillary effects and the three-phase flow hydrodynamics are resolved. An appropriate repulsive interparticle collision force has been suggested to counteract the short-range capillary attraction caused by the depletion layer adjacent to the particle boundary. This short-range capillary attraction, even though its effect can be diminished with a finer grid resolution, is inevitable when employing a diffuse interface model. In a second stage the effect of the particle concentration on the terminal velocity of a rising fluid droplet is investigated. We have found that, in the Stokes regime, the bubble terminal velocity decreases exponentially with the particle concentration. Further work will include an appropriate extension of the current model to achieve large density and viscosity ratios similar to those observed in industrial air-water systems.

ACKNOWLEDGMENTS

This work was supported by a Marie Curie International Outgoing Fellowship with the European Union Seventh Framework Program for Research and Technological Development (2007–2013) under the grant agreement number 623518.

APPENDIX A: FREE ENERGY DENSITY

The free energy density is here given by

$$f = f_b + \frac{\xi^2}{2} |\nabla(\phi_A - \phi_B)|^2 + \frac{\xi_A^2}{2} |\nabla(\phi_A - \phi_S)|^2 + \frac{\xi_B^2}{2} |\nabla(\phi_B - \phi_S)|^2, \quad (A1)$$

where $f_b = -A(\phi_S)\psi^2/2 + B(\phi_S)\psi^4/4$ [19,20]. The two polynomial expressions $A(\phi_S)$ and $B(\phi_S)$ are derived from a fourth-order expansion of the logarithmic expression $f_b = \phi_A \ln(\phi_A) + \phi_B \ln(\phi_B) + \chi \phi_A \phi_B$, where χ is a parameter describing the affinity between the two fluid constituents. The three tunable interfacial length scales ξ , ξ_A , and ξ_B preceding the gradient terms are introduced to control the particle wettability.

APPENDIX B: SMOOTH PARTICLE PROFILE

The following mathematical function is used to represent the spherical shape of the s th particle:

$$\phi_s(\mathbf{x}) = \begin{cases} 1 & \text{if } |\boldsymbol{\ell}_s| < r_s - \frac{\xi_c}{2} \\ 0 & \text{if } |\boldsymbol{\ell}_s| > r_s + \frac{\xi_c}{2}, \\ \frac{1}{2} \tanh\left(\frac{r_s - |\boldsymbol{\ell}_s|}{\xi_s/2}\right) + \frac{1}{2} & \text{elsewhere} \end{cases} \quad (\text{B1})$$

where r_s is the particle radius, $\boldsymbol{\ell}_s(\mathbf{x}) = \mathbf{x} - \mathbf{X}_s$ the distance vector from the center of mass \mathbf{X}_s of the s th particle to the spatial coordinate \mathbf{x} , and ξ_c the cutoff length.

APPENDIX C: DENSITY AND VISCOSITY FIELDS

The volume fractions ϕ_A and ϕ_B do not actually appear in our implementation, since we introduced the order parameter $\psi(\mathbf{x}, t)$. Since we define $\psi = \phi_A - \phi_B$ and $\phi_A + \phi_B + \phi_S = 1$, the two volume fractions are given by $\phi_A = (1 + \psi - \phi_S)/2$ and $\phi_B = (1 - \psi - \phi_S)/2$. In this way, the total density field is recast as

$$\rho(\psi, \phi_S) = \left(\frac{\rho_A + \rho_B}{2}\right) + \left(\frac{\rho_A - \rho_B}{2}\right)\psi + \left(\rho_S - \frac{\rho_A + \rho_B}{2}\right)\phi_S. \quad (\text{C1})$$

In the absence of a particle, i.e., $\phi_S = 0$, the density reduces to $\rho(\psi = 1, 0) = \rho_A$ in the fluid A and to $\rho(\psi = -1, 0) = \rho_B$ in fluid B. While inside the particle, i.e., $\phi_S = 1$, the density reduces to $\rho(\psi = 0, 1) = \rho_S$. Across an interface, the density smoothly transitions. Similar conclusions can be drawn for the density.

APPENDIX D: NUMERICAL METHOD

The numerical method is briefly described. For a more complete description the reader is referred to our previous work [19–21]. Let ψ^n be the order parameter at the time t^n . The field ψ^{n+1} is first advanced in time using a forward Euler method as

$$\psi^{n+1} = \psi^n - \int_{t^n}^{t^{n+1}} \nabla \cdot \mathbf{J}^n dt, \quad (\text{D1})$$

where $\mathbf{J}^n = \psi^n \mathbf{u}^n - M(\mathbf{I} - \mathbf{n}_S^n \otimes \mathbf{n}_S^n) \cdot \nabla \mu^n$. The position of each center of mass \mathbf{X}_s along with the quaternion \mathbf{Q}_s associated with the s th solid particle is then updated in time as

$$\mathbf{X}_s^{n+1} = \mathbf{X}_s^n + \int_{t^n}^{t^{n+1}} \mathbf{V}_s^n dt, \quad (\text{D2})$$

$$\mathbf{Q}_s^{n+1} = \mathbf{Q}_s^n + \frac{1}{2} \int_{t^n}^{t^{n+1}} \mathbf{A}_s^n \cdot \mathbf{Q}_s^n dt, \quad (\text{D3})$$

where $\mathbf{A}_s(\boldsymbol{\Omega}_s)$ is a 4×4 orthogonal matrix function of the particle rotational velocity [20]. After updating all the solid volume fractions $\phi_{s \in \mathcal{S}}^{n+1}$ [Eq. (B1)] and the summation ϕ_S^{n+1} [Eq. (3)], the density field η^{n+1} and the viscosity field ρ^{n+1} can be advanced in time using Eq. (C1). A fractional step approach is employed here to solve the momentum equation (4). An intermediate velocity is first calculated as

$$\mathbf{u}^* = \mathbf{u}^n + \int_{t^n}^{t^{n+1}} \left\{ -(\mathbf{u}^n \cdot \nabla) \mathbf{u}^n + \frac{1}{\rho^{n+1}} [\nabla \cdot (-p^* \mathbf{I} + \boldsymbol{\sigma}_v^n) - \psi^{n+1} \nabla \mu^{n+1}] \right\} dt, \quad (\text{D4})$$

where p^* is an intermediate pressure calculated by solving a Poisson equation $\nabla \cdot \mathbf{u}^* = 0$ and $\boldsymbol{\sigma}_v^n = \eta^{n+1} [\nabla \mathbf{u}^n + (\nabla \mathbf{u}^n)^\top]$ is the viscous stress tensor. A successive over-relaxation method is employed here to solve the Poisson equation. Note that this solver along with some of the discretization

schemes used in the modified Cahn-Hilliard equation are not optimal. The implementation of a more advanced numerical procedure [40] is, however, well involved. The translational and rotational velocities of the each particle are then updated in time as

$$\mathbf{V}_s^{n+1} = \mathbf{V}_s^n + \frac{1}{m_s} \int_{t^n}^{t^{n+1}} (\sum \mathbf{F}) dt, \quad (\text{D5})$$

$$\mathbf{\Omega}_s^{n+1} = \mathbf{\Omega}_s^n + \mathbf{I}_s^{-1} \cdot \int_{t^n}^{t^{n+1}} (\sum \mathbf{T}) dt. \quad (\text{D6})$$

The hydrodynamic force and torque are derived by assuming a momentum conservation between the particle and the binary fluid. Since the hydrodynamic and the capillary contributions are accounted for in the calculation of the intermediate velocity, the following two time integrals are given by

$$\int_{t^n}^{t^{n+1}} (\mathbf{F}_{\text{hyd}} + \mathbf{F}_{\text{cap}}) dt = \int_{\mathcal{V}} \rho^{n+1} (\delta \mathbf{u}_s^*) d\mathbf{x}, \quad (\text{D7})$$

$$\int_{t^n}^{t^{n+1}} (\mathbf{T}_{\text{hyd}} + \mathbf{T}_{\text{cap}}) dt = \int_{\mathcal{V}} \rho^{n+1} \boldsymbol{\ell}_s^{n+1} \times (\delta \mathbf{u}_s^*) d\mathbf{x}, \quad (\text{D8})$$

where $\delta \mathbf{u}_s^* = \phi_s^{n+1} (\mathbf{u}^* - \mathbf{u}_s^*)$ and $\mathbf{u}_s^* = \mathbf{V}_s^n + \mathbf{\Omega}_s^n \times \boldsymbol{\ell}_s^{n+1}$. Finally the velocity field of the entire Lagrangian particle cloud is enforced onto the total fluid velocity field as

$$\mathbf{u}^{n+1} = \mathbf{u}^* + \int_{t^n}^{t^{n+1}} \left(-\frac{1}{\rho^{n+1}} \nabla p_S + \phi_S \mathbf{f}_S \right) dt, \quad (\text{D9})$$

where the pressure p_S is obtained from the incompressibility condition $\nabla \cdot \mathbf{u}^{n+1} = 0$. The time integral of the force density field is calculated as

$$\int_{t^n}^{t^{n+1}} \phi_S \mathbf{f}_S dt = \phi_S^{n+1} (\mathbf{u}_S^{n+1} - \mathbf{u}^*), \quad (\text{D10})$$

where $\phi_S^{n+1} \mathbf{u}_S^{n+1} = \sum \phi_s^n (\mathbf{V}_s^{n+1} + \mathbf{\Omega}_s^{n+1} \times \boldsymbol{\ell}_s^{n+1})$.

APPENDIX E: THEORETICAL TERMINAL BUBBLE VELOCITY

The theoretical terminal velocity U_b^{th} of a spherical bubble with radius r_b rising in a cubic periodic domain is calculated as

$$\frac{U_b^{\text{th}}|_{3\text{D}}}{|\mathbf{F}_{\text{ext}}|/(6\pi\eta_A r_b)} = 1 - 1.7601c^{1/3} + c - 1.5593c^2, \quad (\text{E1})$$

where $c = \int \phi_B d\mathbf{x} / \int d\mathbf{x}$ is the fraction of space occupied by the bubble volume and $\mathbf{F}_{\text{ext}} = (\rho_B - \rho_A) \mathbf{g} \int \phi_B d\mathbf{x}$ is the external buoyancy force [31]. In a two-dimensional periodic square domain, the theoretical terminal velocity is given by

$$\frac{U_b^{\text{th}}|_{2\text{D}}}{|\mathbf{F}_{\text{ext}}|/(4\pi\eta_A L_0)} = -0.5 \log(c) - 0.738 + c. \quad (\text{E2})$$

The above expressions are valid for $c < 0.25$ [32].

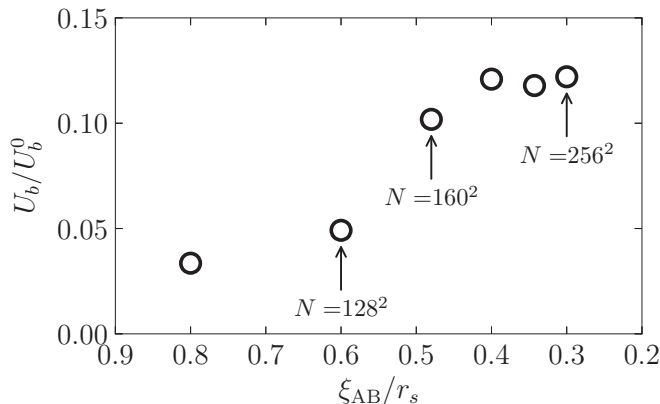


FIG. 9. Effect of the interfacial-length-to-particle-radius ξ_{AB}/r_s on the terminal velocity of a rising droplet. The two-dimensional convergence study was performed with $N_s = 22$ particles.

APPENDIX F: CONVERGENCE STUDY (S5)

We first recall that the field ψ , associated with the A/B interface, varies over the interfacial length [20],

$$\xi_{AB} = \sqrt{\frac{4\xi^2 + \xi_A^2 + \xi_B^2}{\chi - 2}}, \quad (\text{F1})$$

and each solid fraction ϕ_s over the distance ξ_s . These two interfacial lengths here have equal values, i.e., they are set to $\xi_{AB} = \xi_s = 3\Delta$, where Δ is the grid spacing. In the following convergence study, the ratio of the interfacial length to the particle radius ξ_{AB}/r_s is gradually decreased to approach the sharp interface limit. For each simulation in set S5, we set the droplet Reynolds number to $Re_b = 0.98$ and the Etövös number to $Eo_b = 0.23$. As seen in Fig. 9, below a ratio $\xi_{AB}/r_s < 4$, the terminal velocity is no longer affected by the grid density. In the simulations presented in the paper, we chose a grid resolution of $N = 160^2$ in two dimensions and $N = 160^3$ in three dimensions, since it reached a good trade-off between computational cost and result accuracy.

-
- [1] N. Taccoen, F. Lequeux, D. Z. Gunes, and C. N. Baroud, Probing the Mechanical Strength of an Armored Bubble and its Implication to Particle-Stabilized Foams, *Phys. Rev. X* **6**, 011010 (2016).
 - [2] Y. E. Yu, S. Khodaparast, and H. A. Stone, Armoring confined bubbles in the flow of colloidal suspensions, *Soft Matter* **13**, 2857 (2017).
 - [3] S. Y. Tan, S. Ata, and E. J. Wanless, Direct observation of individual particle armored bubble interaction, stability, and coalescence dynamics, *J. Phys. Chem. B* **117**, 8579 (2013).
 - [4] G. Lecrivain, G. Petrucci, M. Rudolph, U. Hampel, and R. Yamamoto, Attachment of solid elongated particles on the surface of a stationary gas bubble, *Int. J. Multiphase Flow* **71**, 83 (2015).
 - [5] B. D. Johnson and R. C. Cooke, Generation of stabilized microbubbles in seawater, *Science* **213**, 209 (1981).
 - [6] K. Stratford, R. Adhikari, I. Pagonabarraga, and J. C. Desplat, Lattice Boltzmann for binary fluids with suspended colloids, *J. Stat. Phys.* **121**, 163 (2005).
 - [7] G. B. Davies, T. Kruger, P. V. Coveney, and J. Harting, Detachment energies of spheroidal particles from fluid-fluid interfaces, *J. Chem. Phys.* **141**, 154902 (2014).

- [8] H. I. Mehrabian, J. Harting, and J. H. Snoeijer, Soft particles at a fluid interface, *Soft Matter* **12**, 1062 (2016).
- [9] T. Krüger, S. Frijters, F. Günther, B. Kaoui, and J. Harting, Numerical simulations of complex fluid-fluid interface dynamics, *Eur. Phys. J.: Spec. Top.* **222**, 177 (2013).
- [10] X. C. Luu and A. Striolo, Ellipsoidal Janus nanoparticles assembled at spherical oil/water interfaces, *J. Phys. Chem. B* **118**, 13737 (2014).
- [11] M. van Sint Annaland, N. G. Deen, and J. A. M. Kuipers, Numerical simulation of gas-liquid-solid flows using a combined front tracking and discrete particle method, *Chem. Eng. Sci.* **60**, 6188 (2005).
- [12] S. Sasic, E. K. Sibaki, and H. Ström, Direct numerical simulation of a hydrodynamic interaction between settling particles and rising microbubbles, *Eur. J. Mech. B* **43**, 65 (2014).
- [13] S. Bogner, J. Harting, and U. Rüde, Direct simulation of liquid-gas-solid flow with a free surface lattice Boltzmann method, *Intl. J. Comput. Fluid Dyn.* **31**, 463 (2017).
- [14] D. M. Anderson, G. B. McFadden, and A. A. Wheeler, Diffuse interface model methods in fluid mechanics, *Annu. Rev. Fluid Mech.* **30**, 139 (1998).
- [15] T. Araki and H. Tanaka, Wetting-induced depletion interaction between particles in a phase-separating liquid mixture, *Phys. Rev. E* **73**, 061506 (2006).
- [16] P. C. Millett and Y. U. Wang, Diffuse-interface field approach to modeling arbitrarily-shaped particles at fluid-fluid interfaces, *J. Colloid Interface Sci.* **353**, 46 (2011).
- [17] H. Shinto, Computer simulation of wetting, capillary forces, and particle-stabilized emulsions: From molecular-scale to mesoscale modeling, *Adv. Powder Tech.* **23**, 538 (2012).
- [18] T. Cheng and Y. U. Wang, Shape-anisotropic particles at curved fluid interfaces and role of Laplace pressure: A computational study, *J. Colloid Interface Sci.* **402**, 267 (2013).
- [19] G. Lecrivain, R. Yamamoto, U. Hampel, and T. Taniguchi, Direct numerical simulation of a particle attachment to an immersed bubble, *Phys. Fluids* **28**, 083301 (2016).
- [20] G. Lecrivain, R. Yamamoto, U. Hampel, and T. Taniguchi, Direct numerical simulation of an arbitrarily shaped particle at a fluidic interface, *Phys. Rev. E* **95**, 063107 (2017).
- [21] Y. Nakayama and R. Yamamoto, Simulation method to resolve hydrodynamic interactions in colloidal dispersions, *Phys. Rev. E* **71**, 036707 (2005).
- [22] J. Molina and R. Yamamoto, Direct numerical simulations of rigid body dispersions. I. Mobility/friction tensors of assemblies of spheres, *J. Chem. Phys.* **139**, 234105 (2013).
- [23] A. Esmaeeli and G. Tryggvason, A direct numerical simulation study of the buoyant rise of bubbles at $O(100)$ Reynolds number, *Phys. Fluids* **17**, 093303 (2005).
- [24] G. Lecrivain, R. Rayan, A. Hurtado, and U. Hampel, Using quasi-DNS to investigate the deposition of elongated aerosol particles in a wavy channel flow, *Comput. Fluids* **124**, 78 (2016).
- [25] G. Bournival, S. Ata, and E. J. Wanless, The roles of particles in multiphase processes: Particles on bubble surfaces, *Adv. Colloid Interf. Sci.* **225**, 114 (2015).
- [26] X. Sun and M. Sakai, Direct numerical simulation of gas-solid-liquid flows with capillary effects: An application to liquid bridge forces between spherical particles, *Phys. Rev. E* **94**, 063301 (2016).
- [27] D. S. Bolintineanu, G. S. Grest, J. B. Lechman, F. Pierce, S. J. Plimpton, and P. R. Schunk, Particle dynamics modeling methods for colloid suspensions, *Comput. Particle Mech.* **1**, 321 (2014).
- [28] R. Chella and J. Vinals, Mixing of a two-phase fluid by cavity flow, *Phys. Rev. E* **53**, 3832 (1996).
- [29] V. E. Badalassi, H. D. Ceniceros, and S. Banerjee, Computation of multiphase systems with phase field models, *J. Comput. Phys.* **190**, 371 (2003).
- [30] M. K. Tripathi, K. C. Sahu, and R. Govindarajan, Dynamics of an initially spherical bubble rising in quiescent liquid, *Nat. Commun.* **6**, 6268 (2015).
- [31] H. Hasimoto, On the periodic fundamental solutions of the Stokes equations and their application to viscous flow past a cubic array of spheres, *J. Fluid Mech.* **5**, 317 (1959).
- [32] A. S. Sangani and A. Acrivos, Slow flow through a periodic array of spheres, *Int. J. Multiphase Flow* **8**, 343 (1982).
- [33] F. Raymond and J. M. Rosant, A numerical and experimental study of the terminal velocity and shape of bubbles in viscous liquids, *Chem. Eng. Sci.* **55**, 943 (2000).

- [34] S. Hysing, S. Turek, D. Kuzmin, N. Parolini, E. Burman, S. Ganesan, and L. Tobiska, Quantitative benchmark computations of two-dimensional bubble dynamics, *Intl. J. Numer. Methods Fluids* **60**, 1259 (2009).
- [35] See Supplemental Material at <http://link.aps.org/supplemental/10.1103/PhysRevFluids.3.094002> for three-dimensional simulation of a droplet rising across a particle cloud.
- [36] N. Hooshyar, J. R. van Ommen, P. J. Hamersma, S. Sundaresan, and R. F. Mudde, Dynamics of Single Rising Bubbles in Neutrally Buoyant Liquid-Solid Suspensions, *Phys. Rev. Lett.* **110**, 244501 (2013).
- [37] M. W. Baltussen, J. A. M. Kuipers, and N. G. Deen, Direct numerical simulation of effective drag in dense gas-liquid-solid three-phase flows, *Chem. Eng. Sci.* **158**, 561 (2017).
- [38] S. Mueller, E. W. Llewellyn, and H. M. Mader, The rheology of suspensions of solid particles, *Proc. R. Soc. London A* **466**, 1201 (2010).
- [39] A. Einstein, Berichtigung zu meiner Arbeit: Eine neue Bestimmung der Moleküldimensionen, *Ann. Phys.* **339**, 591 (1911).
- [40] M. Fujita, O. Koike, and Y. Yamaguchi, Direct simulation of drying colloidal suspension on substrate using immersed free surface model, *J. Comput. Phys.* **281**, 421 (2015).